Research Article Vol. 2, No. 6 / 15 June 2019 / *OSA Continuum* 2038

OSA CONTINUUM

Digital coronography: application to space telescope images

P. J. Valle,[1] A. Fuentes,[1] V. F. Canales,[1] M. A. Cagigas,[2,*] and M. P. Cagigal[1]

[1] *Dept. de Física Aplicada, Universidad de Cantabria, Avenida de los Castros 48, 39005 Santander, Spain*
[2] *Instituto de Astrofísica de Canarias, Vía Lactea s/n, 38200 La Laguna, Spain*
[*] *mcagigas@iac.es*

Abstract: Optical coronagraphy is a high contrast image technique used in astronomy to reduce light around a host star and make viable the detection of faint companions and the exploration of circumstellar disks. Digital coronagraphy consists of the digital processing of non-coronagraphic images acquired by space telescopes in order to reproduce the operation of a standard optical coronagraph. Digital coronagraphy presents significant advantages as no real coronagraph or extra device has to be manufactured and sent to space. In this paper, comparison of digital and optical coronagraph performances is accomplished both by numerical simulations that include detection noise and the use of archived images from the Hubble Space Telescope. Our analysis indicates that the attainable contrast with both techniques is comparable, though the required Lyot stop in digital coronagraphy differs from the standard one. Furthermore, the evolution of contrast as a function of the distance to the main star that we have encountered with the optical coronagraph is similar to that shown by different authors for the optical NIC2/COR coronagraph. Finally, although digital coronagraphy cannot substitute optical coronagraphs, it can be considered as an interesting tool for the analysis of actual system performance.

1. Introduction

Imaging of stellar faint companions and circumstellar disks are relevant topics that can be addressed by optical coronagraphs (OC) [1–4]. However, this technique is not feasible unless aberrations caused by atmospheric turbulence are removed. The most evident strategy is to implement the coronagraph at a space telescope. This option presents relevant drawbacks: an enormous cost, the design for a challenging environment as space, the implementation into a space craft, the launch to space, the extreme difficulty of later modifications, etc. In a previous paper [5], we introduced a technique, the Digital Coronagraphic Algorithm (DCA), which emulates the optical coronagraphic operation in standard images of a telescope. The technique was shown to achieve a speckle noise reduction comparable to that of an actual coronagraph and was checked by a laboratory experiment. The aim of this paper is to show the use of the DCA technique on images previously acquired by space telescopes since it presents several advantages. For example, no coronagraph or extra device has to be manufactured, different coronagraphic masks and Lyot stops can be tested on each target, pointing errors and misalignment due to stress are avoided, wavefront aberrations due to alignment errors are cancelled out, no coronagraph has to be sent to space and chromatic aberrations are minimized. On the other hand, the main drawback is the limited dynamic range of the scientific camera although this problem may be overcome if image acquisition is properly prepared. It is important to note that images from DCA can benefit from other post processing techniques usually applied to space telescope images, like Angular Differential Imaging algorithm [6], Locally Optimized Combination of Images (LOCI) algorithm [7] or Karhunen-Loeve Image Projection (KLIP) algorithm [8].

This paper is organized as follows. In section 2, we review the DCA theoretical foundation and show how star and companion signals are processed. In section 3, DCA and OC contrast

#364424 https://doi.org/10.1364/OSAC.2.002038
Journal © 2019 Received 9 Apr 2019; revised 16 May 2019; accepted 16 May 2019; published 13 Jun 2019

achievements are compared under ideal conditions and we find that the DCA requires an external Lyot stop, in contrast to the inner one used in the OC. In section 4, computer simulations have been carried out to compare OC and DCA behavior when detection noise is considered. In section 5, DCA has been applied to images detected by the Hubble Space Telescope (HST). The results are compared to those produced by the on board NIC2/COR optical coronagraph. Finally, the main conclusions are summarized in section 6.

2. Theoretical framework

DCA deals with already detected images and emulates the steps of the OC. Unlike OC, DCA starts from intensity images, and the key of the algorithm is to convert such intensity images into amplitude ones. To compare the behavior of OC and DCA we use a one-dimensional scheme [9]. In an OC, Fig. 1, the optical field at the entrance pupil plane (a) is Fourier transformed by the first lens to produce a field distribution at the coronagraphic plane (b) which, once multiplied by the coronagraphic mask, is Fourier transformed by the second lens to produce the field at the Lyot stop plane (c). The third lens performs the last Fourier transform of the field multiplied by the Lyot stop, which yields a final coronagraphic image at the detection plane (d). We will follow an analogous procedure in DCA for both a centered and a non-centered source.

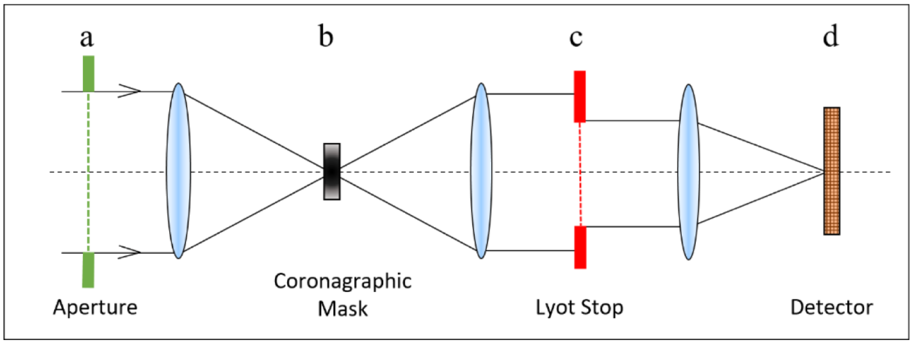

Fig. 1. Standard optical coronagraph. a: entrance pupil plane, b: coronagraphic plane, c: Lyot stop plane, d: detection plane.

2.1. *Centered star*

Let us assume a circular clear pupil and a centered star. Fig. 2a shows the field amplitude at the telescope entrance pupil. The field distribution at the coronagraphic plane (Fig. 2b-left), which corresponds to the amplitude point spread function of the telescope, is described by $APSF(r) \propto J_1(r)/r$, where J_1 is the first order Bessel function of the first kind and r the distance to the center (axis of the optical system). This function quasiperiodically takes positive and negative values, with a period related to λ/D, where λ is the detection wavelength and D the telescope aperture size. In the optical coronagraph, a mask multiplies this field to cancel out the central peak. In the Lyot plane, the light around the pupil border is reduced by means of the Lyot stop (Fig. 2c-left). Fig. 2d-left shows the detected image that yields the coronagraph. The result is a considerable reduction of the light around the star (unit intensity corresponds to the non-coronagraphic star image peak), which increases the contrast and, consequently, the companion detectability. DCA algorithm emulates this process for images detected at the telescope image plane. Fig. 2b0-right shows the detected image PSF of the centered star, whose intensity is described by $I(r) = |APSF(r)|^2$. To reproduce the operation that takes place along a coronagraph, the first step is to recover the star image field from the star image intensity. Given that both $APSF(r)$ and $|APSF(r)|^2$ are real functions, it is enough to multiply the root square of the detected star intensity, *I(r)*, by the real function *S(r)*, which provides the sign distribution lost at the detection process:

$$\boldsymbol{A}(\boldsymbol{r}) \propto \sqrt{\boldsymbol{I}(\boldsymbol{r})}\boldsymbol{S}(\boldsymbol{r}) \tag{1}$$

where *S(r)* is defined as:

$$\boldsymbol{S}(\boldsymbol{r}) = \frac{\boldsymbol{APSF}\ (\boldsymbol{r})}{|\boldsymbol{APSF}\ (\boldsymbol{r})|} \tag{2}$$

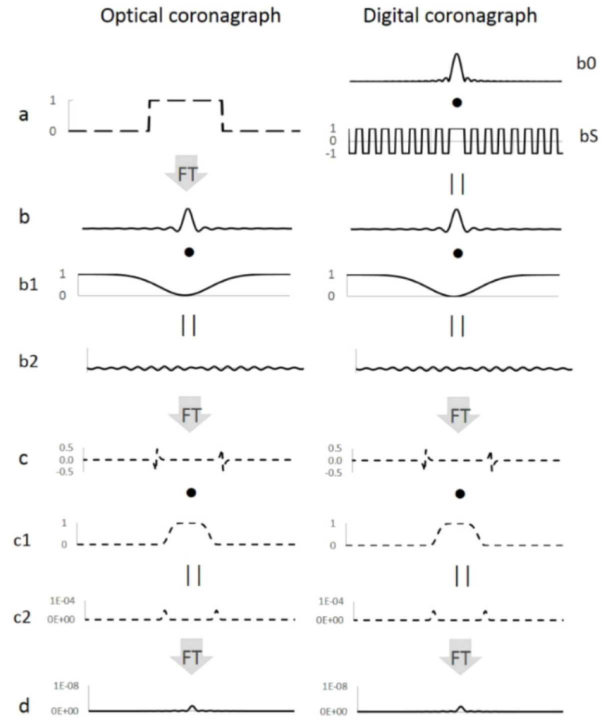

Fig. 2. One-dimensional summary of profiles at the same planes of Fig. 1 for the optical coronagraph (left) and comparison with the digital coronagraph (right). Note that b0 represents the intensity, bS the sign map and b1 the mask at the coronagraphic plane, and c1 the Lyot stop.

For a clear circular aperture $S(r) = J_1(r)/|J_1(r)|$ and it consists on a series of annuli that take values of 1 or -1, as is shown in Fig. 3-left. In pupil geometries that include a central obscuration, the function is still binary but the annuli distribution will depend on the inner and outer pupil radii. Figure 3-right shows an example of the sign map for a pupil with central obscuration. Fig. 2b-left and Fig. 2b-right represent a comparison between the direct *APSF* obtained in the optical coronagraph and that obtained from Eq. (1). We can see that both functions are identical. From this point, the rest of the process that takes place in an optical coronagraph can be reproduced by using numeric Fourier transforms [10] and digitally defined coronagraphic masks and Lyot stops.

2.2. Stellar companion

A general image containing some other objects than a centered star, requires additional considerations. In the case of a host star and a weak companion, the detected image includes the star intensity $I_S(r)$ and the companion intensity $I_C(r\text{-}r_0)$, where r_0 is the distance from the companion

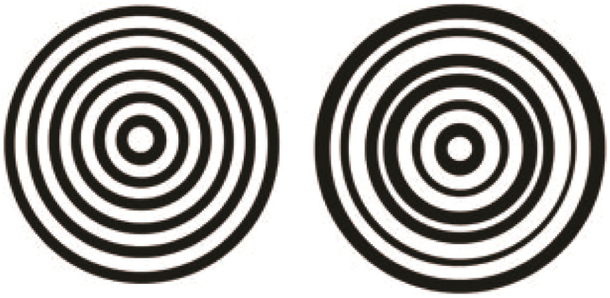

Fig. 3. Binary sign map given by Eq. (2) for a pupil without central obscuration (left) and with central obscuration (right). Value + 1 is represented by white regions while value -1 by black ones.

to the host star. When we multiply the square root of the detected image intensity by the sign map given by Eq. (2), we can approximate [11]:

$$A(r) \approx \sqrt{I_S(r)}S(r) + \frac{I_C(r - r_0)S(r)}{2\sqrt{I_S(r)}} \tag{3}$$

There are two contributions for this field. The contribution due to the star light *sqrt* $(I_S(r)).S(r)$ is the only relevant one except at the companion location ($r = r_0$). Let us note in Eq. (3) that the centers of symmetry of $I_C(r\text{-}r_0)$ and $S(r)$ are at separate positions, so that the field companion in this case is not perfectly recovered from the intensity. The field from Eq. (3) is multiplied by the coronagraphic mask and Fourier transformed, to obtain the field at the Lyot plane. In this plane, star light is distributed around the pupil border (Fig. 4-a) but an important fraction of the companion energy is diffracted outside the entrance pupil (Fig. 4-b) since the displaced sign map works as a diffraction grating for the companion light. Consequently, it is important to find out the Lyot stop shape that will best perform in DCA (this is discussed in the next section).

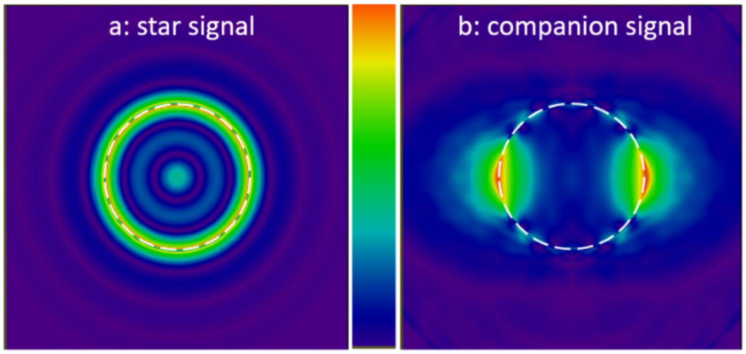

Fig. 4. Outline of the dissimilar spatial spread of both contributions at the Lyot plane, a: star, b: companion. The companion is 100 times fainter than the host star and is placed at 13 λ/D.

So far we have considered monochromatic wavelength, but actual imaging systems work on wavelength bands. In this context, the advantage of the digital coronagraph is that, unlike the optical coronagraph, coronagraphic masks and lenses do not introduce any additional chromatic dispersion. Of course, the detected image presents a combination of images that correspond to wavelengths in the detection band, so that the sign map shown in Fig. 3 must be an average of the sign maps given by Eq. (2) for that band.

OSA CONTINUUM

3. Contrast curves

3.1. DCA and OC contrast

Let us first analyze the ideal behavior of DCA in order to uncover its performance limits and to study the best Lyot stop shape. As we mentioned in the previous section, in the Lyot plane, part of the companion light is spread outside the pupil area (Fig. 4-b) unlike the centered star light which is concentrated around the pupil border. To take advantage of this fact we suggest to use an external Lyot stop, i.e., a Lyot stop with transmittance in the region outside the pupil area (as opposed to an optical device this is possible in a digital process). Theoretical contrast curves can be used to compare the performances of DCA with inner and outer Lyot stops with that of the OC. In this calculation, we do not consider any kind of noise so a perfect incident plane wave from a centered star is assumed. In an OC, the contrast radial dependence can be defined as [12]:

$$C(r) = \frac{I(r)}{|M(r)|^2 I_S(0)} \tag{4}$$

where $I(r)$ is the intensity at the radial coordinate in the final image, $I_S(0)$ is the peak stellar intensity measured without the image mask in the optical train and $|M(r)|^2$ is the mask intensity transmission. However, for the DCA, the companion peak intensity in the final image will depend on its position, because the sign map is not centered at the companion location. Then, it is more convenient for the contrast to use the expression:

$$C'(r) = \frac{I(r)}{|M(r)|^2 I_C(r)} \tag{5}$$

where $I_C(r)$ is the intensity of a star with the same intensity as the host star but placed at a distance r from it.

We consider an annular entrance pupil like that of the HST (with a central obscuration diameter $0.33D$). The coronagraphic mask is a 2.2 λ/D radius hard edge opaque disk (equivalent to the coronagraphic hole of the instrument NICMOS in HST). The Lyot stop transmittance is given by a super-Gaussian annulus function:

$$SG(r,n) = exp\left(-\left|\frac{r-r_0}{\sigma}\right|^{2n}\right) \tag{6}$$

where σ is the half-width, r is the usual radial coordinate and r_0 is the central radius of the super-Gaussian annulus. We use two different types of super-Gaussian Lyot stops, the first one is inside the entrance pupil (Fig. 5-a) and the second one is outside the entrance pupil (Fig. 5-b). We calculate contrast values of DCA using both Lyot stops and compare them with that of the OC (OC Lyot stop is a hard edge annular pupil with $0.35D$ inner and $0.94D$ external diameters). A major advantage of DCA method is that several Lyot stop parameters can be easily checked looking for the values providing better contrast. Figure 6 shows the comparison the OC contrast curve (red line) calculated according to Eq. (4) and averaged DCA contrast curves calculated using Eq. (5) for inner (green line) and outer (blue line) Lyot stops. The mean values of the parameters for of inner and outer Lyot stops are $r_0 = 0.32D$, $\sigma = 0.12D$ and $r_0 = 0.85D$, $\sigma = 0.25D$, respectively (in both cases $n = 6$, see [13]). We can see that the DCA contrast with inner Lyot does not improve the OC contrast but outer Lyot shows better contrast than OC. Consequently, the DCA is comparable to the OC if the outer Lyot stop is used. Let us note that these theoretical contrast values could even be improved using other coronagraphic masks like phase quadrant or vortex masks (note that contrast ratios of the order of 104 for small angular resolution, within the fourth Airy ring, have been realized with such masks).

OSA CONTINUUM

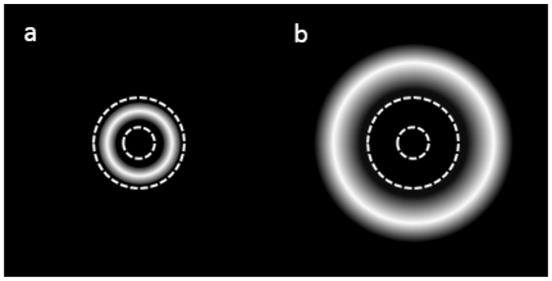

Fig. 5. Representation of super-Gaussian Lyot stops (red) and annular pupil (green). (a) the inner Lyot stop is inside the annular pupil, (b) the outer Lyot stop is outside the pupil area.

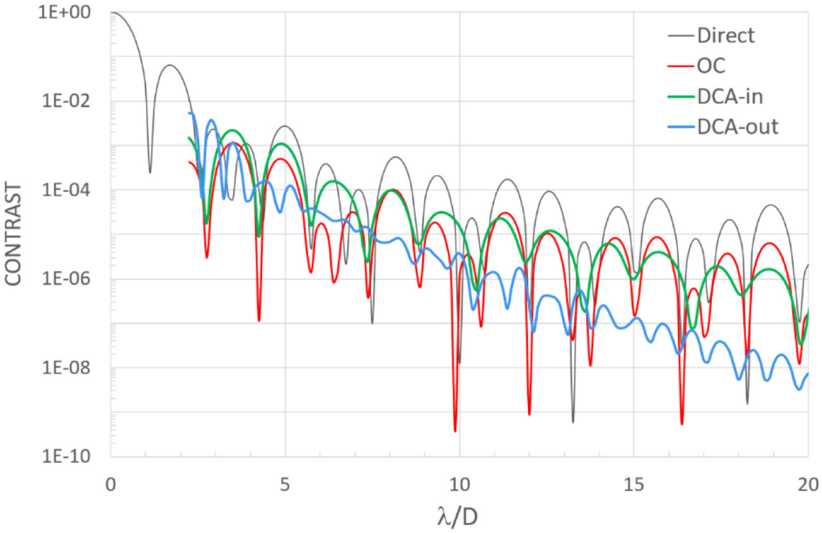

Fig. 6. Contrast curves for the OC (red line) calculated according to Eq. (4) and for the DCA calculated using Eq. (5) with an inner Lyot stop (green line) and with an outer Lyot stop (blue line). Direct star intensity (without coronographic mask) is also shown (black line).

4. Noise reduction

4.1. *Noise analysis*

When dealing with actual astronomical images additional considerations must be made. A first limitation comes from the finite dynamic range of the detecting cameras. The topmost peak intensity of the host star and the camera limited dynamic range determine the minimum detectable object intensity in archived images. Objects with intensity lower than this minimum have been definitively lost. However, to take better advantage of the camera dynamic range, in order to detect fainter objects, it would be enough to mask the host star peak before detection.

A second limitation comes from the noises involved in the detection process like camera electronic noise, Poisson noise and speckle noise. A detection is considered reliable when the object intensity is several (usually three or five) times larger than the surrounding noise standard deviation. Hence, two queries arise about the companion detectability when using DCA. The first one is whether the companion detection is limited by the noise of the direct image or by the noise of the coronagraphic image. The answer is obtained by a numerical simulation shown at the end of this section. The second question is how much the DCA reduces the noise in the final coronagraphic image. In the assumption of low electronic noise, the dominant contribution to the focal plane image noise is the pinned speckle [14]. The reduction of this pinned speckled noise by DCA is comparable to that by OC. In consequence, the remaining pure random speckle noise limits the companion detection similarly in both cases [15]. In order to explain briefly such behavior let us obtain a theoretical expression for the coronagraphic star light intensity. For a real pupil function A, the electric field strength at the pupil will be exp$(-i\phi)$, where ϕ is the pupil wavefront error of the incoming wave (which accounts for the noises in the detection process). Furthermore, space based telescopes may reach very high Strehl ratio values (SR values higher than 0.9) denoting a very low wavefront error. In this conditions, we can approximate exp$(-i\phi)\approx 1-i\phi$ and the non-coronagraphic intensity of the star will be given by:

$$I_S = |\overline{A\mathrm{e}^{-i\phi}}|^2 \approx \overline{|A|}^2 + \overline{|A\phi|}^2 - 2\overline{|A|}\mathrm{Im}\overline{(A\phi)} \tag{7}$$

where the overline stands for Fourier transform. The intensity of the coronagraphic image for the DCA will be:

$$I_{DCA} = \left|\overline{\overline{\overline{|\overline{A\mathrm{e}^{-i\phi}}|SM}L}}\right|^2 \tag{8}$$

where M is the coronagraphic mask, L the Lyot stop and S the sign distribution given by Eq. (2) (coordinate dependence has been omitted to shorten the description). This coronagraphic intensity can be approximated by [16]:

$$I_{DCA} \approx |\bar{A}M * \bar{L}|^2 + |\mathrm{Im}\overline{(A\phi)}M * \bar{L}|^2 - 2(\bar{A}M * \bar{L})(\mathrm{Im}\overline{(A\phi)}M * \bar{L}) \tag{9}$$

where * stands for convolution product. If we compare Eqs. (7) and (9) we can see that the non-aberrated PSF term (the first term) is reduced due to the use of the coronagraphic mask and the Lyot stop, as expected. Besides, the pinned speckled noise term $|\bar{A}|Im(\overline{A\phi})$ is also strongly reduced to $(\bar{A}M * \bar{L})(Im(\overline{A\phi})M * \bar{L})$. Both, host star light cancellation and pinned speckle noise reduction will strongly depend on the mask and Lyot stop used, as in the OC case.

Next, we will show the reduction of these terms by numerical simulation of speckled images generated by incoming aberrated wavefronts [17]. The entrance pupil, coronagraphic mask and Lyot stops were the same as those used in the previous section. A series of 200 aberrated wavefronts providing SR values around 0.9 were used (reasonable SR value for space based telescope images). The intensity standard deviations of the final images as a function of the distance from the stellar peak are calculated (Fig. 7) for the direct image (black line), for the OC (red line), for the DCA with inner Lyot stop (green line) and for the DCA with outer Lyot stop (blue line). We can see that the residual noise standard deviation in the DCA image is lower than that of the OC, specially in the case of the outer Lyot stop. A reduction factor of ten can be attained for distances shorter than $15\lambda/D$. As a consequence, companion detectability is limited by noise in the coronagraphic image instead of that in the direct image and a companion will only be detected when its intensity is larger than the residual random noise intensity standard deviation.

The effect of the noise level is analyzed in Fig. 8 where contrast curves for several Strehl values are shown in the case of DCA with outer Lyot stop. We choose a region of interest with distances between 5 - 20 λ/D from the central star. The great theoretical performance achieved for $SR = 1$ is quickly ruined as SR decreases. This means that high quality images, with a high level of distortion compensation, are required for a successful application of DCA.

OSA CONTINUUM

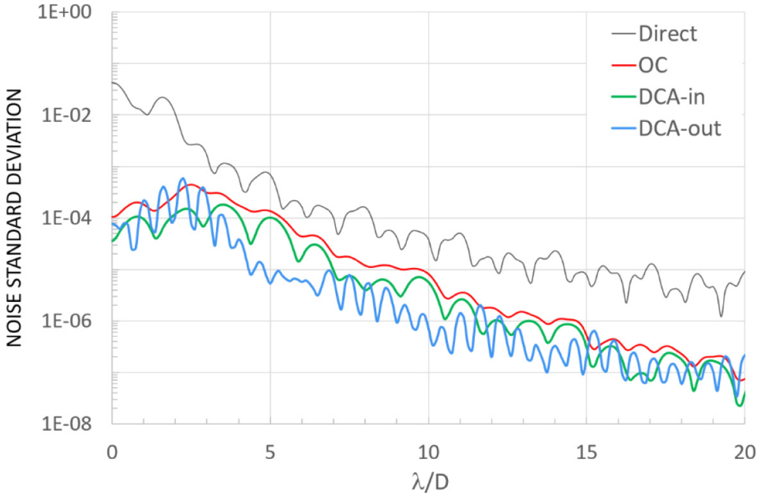

Fig. 7. Noise standard deviation for the OC (red line) and for the DCA with inner Lyot stop (green line) and outer Lyot stop (blue line). Direct intensity star standard deviation is also shown (black line)

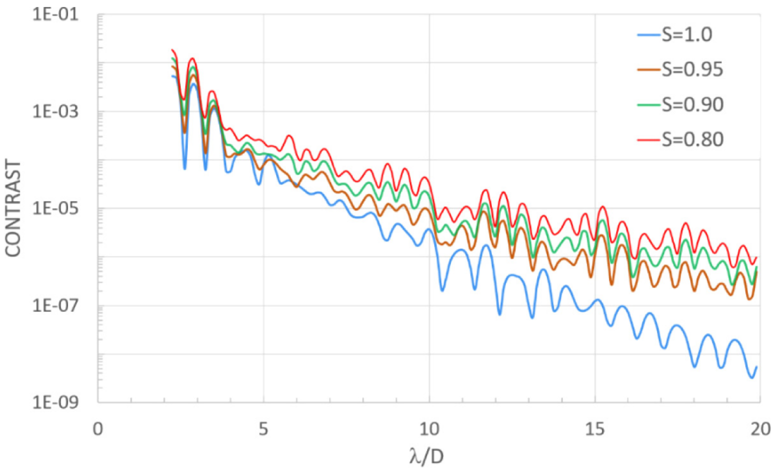

Fig. 8. Contrast curves for the DCA calculated using an outer Lyot stop for wavefronts providing $SR = 1$ (blue line), $SR = 0.95$ (brown line), $SR = 0.90$ (green line) and $SR = 0.80$ (red line)

5. Application to Hubble Space Telescope

5.1. Performance with HST images

To present a more realistic analysis of the algorithm features we have evaluated the rejection factor, the contrast curve and the 3σ-contrast using HST images acquired by cameras NICMOS/NIC1 and NIC2.

We have reproduced the method followed by [18] for estimating the coronagraphic rejection factor of the HST optical coronagraph. The coronagraphic rejection factor is defined as the azimuthally-averaged reduction in the scattered/diffracted circumstellar light background achieved with the coronagraph. Schneider estimated this factor using two different images of the same target. The first one, named direct, is an image obtained through the HST coronagraph without any coronagraphic mask. The second one is a coronagraphic image. Schneider estimates the coronagraphic rejection factor using the images of a bright isolated K5 V star named GJ517. These images were taken by the instrument NICMOS/NIC2 with the filter F160W and calibrated, reduced, and processed by the GO/10177 team. To assess the DCA rejection factor, we applied DCA to the direct image of GJ517 (provided by Schneider). We started from the Airy pattern of the star, then we found the sign map that better fitted with the Airy ring structure and then we performed DCA. In this case, we used a sign map like that shown in Fig. 3-right (annular shaped pupil) to obtain the corresponding digital coronagraphic image. Then the new coronagraphic rejection factor was estimated from direct and DCA images. Figure 9 shows a comparison between the rejection factor achieved by the optical coronagraph NIC2/COR (red line) and DCA (green line). It can be seen that the highest rejection factor corresponds to DCA and that it shows a strong dependence on the angular distance to the host star.

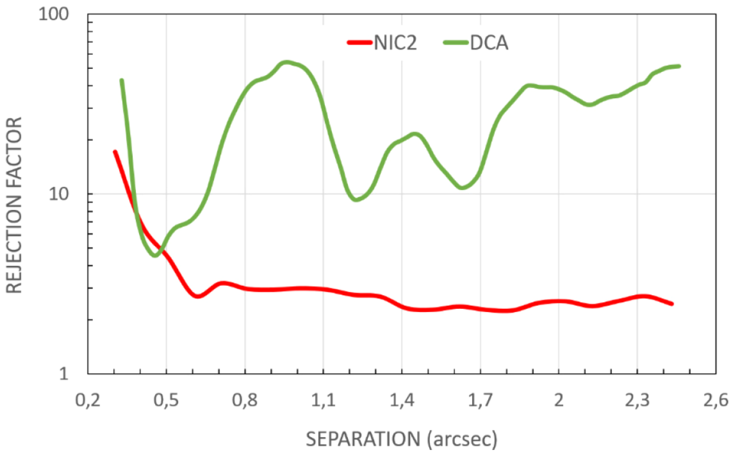

Fig. 9. Coronagraphic rejection factor for star GJ517 for the optical coronagraph NIC2/COR (red line, Schneider) and DCA (green line).

The next step was to estimate the coronagraphic raw contrast achievable by our technique when it is applied to an actual image. For this purpose we used non-coronagraphic images of the star BRI-0021. We selected this target for different reasons. It is a bright star, its images are not saturated and images from the instrument NISMOS/NIC1, NISMOS/NIC2 can be downloaded from the MAST archive. Besides, post-processed images can be downloaded from the ALICE archive [19]. The procedure we followed is the already mentioned one. We started from the Airy pattern of the star, then we found the sign map that better fitted the Airy rings structure and then we used DCA to obtain the corresponding coronagraphic image. This was repeated for images from NIC1 and from NIC2 recorded with the F160W filter. The definition of raw contrast used here is the same as that described by Eq. (5). Dashed green line in Fig. 10 shows the azimuthal average of the NIC1 direct image (non-coronagraphic image) and solid green line shows the coronagraphic raw contrast achieved with DCA. For NIC2 camera, dashed red line shows direct image whilst red solid line shows the raw DCA contrast. It can be seen that although absolute values for each camera are different (probably due to the different pixel scale) the contrast improvement due to DCA presents similar figures for both cameras. The improvement can be roughly stated as a factor of 3 for distances around 0.5’’ and it grows to a factor of 8 for distances larger than 0.8’’. This behavior is similar to that shown by different authors for the optical NIC2/COR coronagraph, see Fig. 1 in [20]. However, a direct comparison between our raw contrast curve and those curves in the literature is difficult since we do not exactly know how the literature curves were obtained and in this case little details may be crucial.

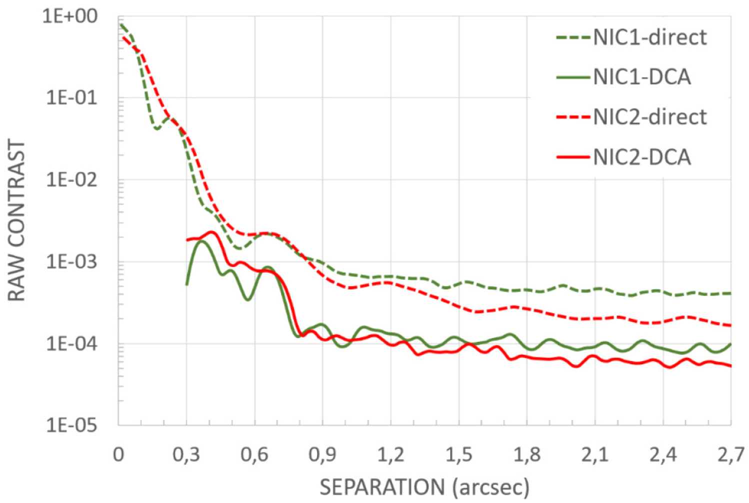

Fig. 10. Contrast curves of star BRI-0021. Dashed-lines are direct non-coronagraphic images and solid-lines are DCA results. NIC1 and NIC2 camera images are green and red lines, respectively.

The contrast as defined by Eq. (4) may not be a reliable parameter when dealing with very noisy images. In these cases it is necessary to define the 3-σ or the 5-σ contrast. The n-contrast is defined as:

$$C_{\sigma}(r) = \frac{n\sigma(r)}{|M(r)|^2 I_S(0)} \tag{10}$$

where $\sigma(r)$ is the local standard deviation of the coronagraphic image, $I_s(0)$ is the peak stellar intensity measured without the mask in the optical train and $|M(r)|^2$ is the mask intensity transmission. Figure 11 shows the 3-σ contrast evaluated from the same images we used for estimating the raw contrast.

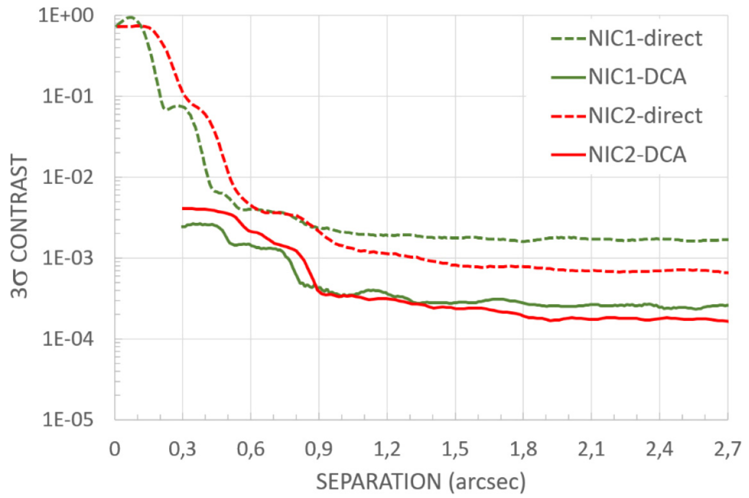

Fig. 11. 3 -σ contrast curves of star BRI-0021. Dashed-lines are direct non-coronagraphic images and solid-lines are DCA results. NIC1 and NIC2 camera images are green and red lines, respectively).

It can be seen that the 3-σ contrast improvement is a factor of about 3 for distances around 0.5'' and it grows up to a factor of 10 for distances larger than 0.8'' for the camera NIC1. The improvement for the NIC2 camera is slightly lower than for NIC1. It is difficult to find contrast curves for the HST NIC2 coronagraph in the literature. Nevertheless, similar values have been achieved by the NIC2 coronagraph under similar (although not identical) recording conditions.

Finally, in order to compare the kind of images provided by DCA, Fig. 12 shows the NIC2/COR image (left) and DCA (right) coronagraphic images of the target GJ517 (10448 2-GYRO GJ 517 21 February 2005). The intensity is in logarithmic scale and the field of view is 6.9'' x 6.9'' in both images. It can be seen that in the DCA image a clear ring structure appears and a higher background light cancellation is achieved. Note that this image is consistent with the results shown in Fig. 9. In this case it is not possible to detect any possible faint companion.

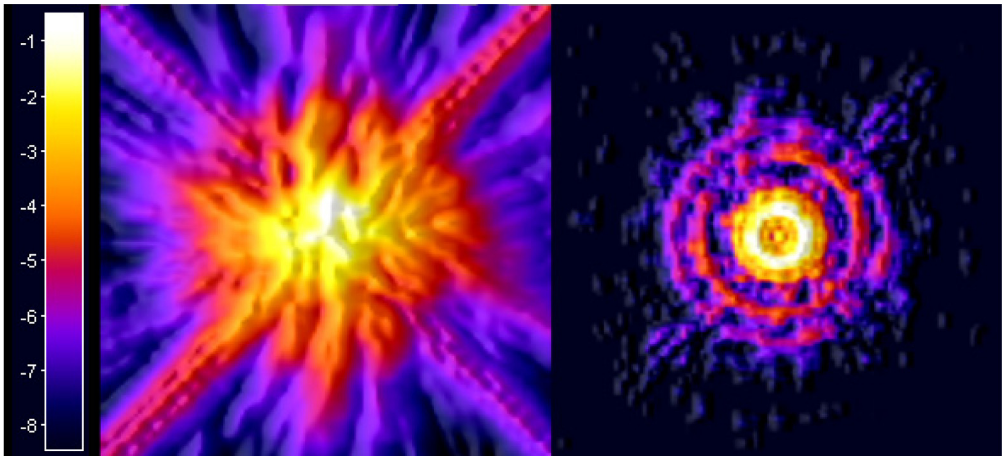

Fig. 12. Optical NIC2/COR (left) and digital DCA (right) coronagraphic images of star GJ517

6. Conclusions

The coronagraph digital algorithm can cancel stellar light in high-quality images in some cases almost as efficiently as an optical coronagraph, with a number of advantages. The sole requirement of the algorithm is the acknowledgement of the amplitude point spread function of the telescope in order to obtain its sign map. From a captured image and the corresponding sign map, the digital algorithm imitates the process that takes place in an optical coronagraph. The results shown in this paper correspond to the combination of hard-edge coronagraphic masks and Super-Gaussian Lyot stops, although many other combinations of coronagraphic masks and Lyot stops are possible as well.

A theoretical analysis of the detection noise behaviour in the digital coronagraph reveals that noise reduction is accomplished in a similar way than in the optical one although residual noise can be lowered by a factor of ten. The algorithm has been checked using experimental HST images. Coronagraphic rejection factor, raw contrast and 3-σ contrast values provided by DCA are similar (or even a little better) than those obtained from the NIC2/COR optical coronagraph. The main limitation when applying DCA to archived images comes from the detection process. Those objects whose intensity was out the camera dynamic range are definitively lost. Nevertheless, to acquire new images that are planned to be processed with DCA, certain strategies can be adopted for a more advantageous use of the camera dynamic range.

A major advantage of DCA is that different coronagraphic masks (vortex, differentiation, band limited, etc.) and Lyot stops (apodized, hard-edge, etc.) can be implemented without the demand of their manufacture. Other important benefits are that pointing and alignment errors are avoided and the processing is not dependent on the wavelength. Finally, in spite of its limitations of the implementation of DCA on actual images, it can become a useful tool to estimate performance in actual systems.

Funding

Ministerio de Economía, Industria y Competitividad, Gobierno de España (AYA2016-78773-C2-1-P).

Acknowledgments

This research has made use of data reprocessed as part of the ALICE program, which was supported by NASA through grants HST-AR-12652 (PI: R. Soummer), HST-GO-11136 (PI: D. Golimowski), HST-GO-13855 (PI: E. Choquet), HST-GO-13331 (PI: L. Pueyo), and STScI Director's Discretionary Research funds, and was conducted at STScI which is operated by AURA under NASA contrast NAS5-26555.

References

1. M. A. Cagigas, P. J. Valle, and M. P. Cagigal, "Super-Gaussian apodization in ground based telescopes for high contrast coronagraph imaging," Opt. Express **21**(10), 12744–12756 (2013).
2. M. A. Cagigas, P. J. Valle, M. P. Cagigal, X. Prieto-Blanco, A. Pérez-Garrido, I. Villo-Pérez, B. Femenía, J. A. Pérez-Prieto, L. F. Rodríguez, R. López, A. Oscoz, and R. Rebolo, "Experimental validation of Lyot stop apodization in ground-based coronagraphy," Mon. Not. R. Astron. Soc. **446**(1), 627–632 (2015).
3. E. Choquet, L. Pueyo, J. B. Hagan, E. Gofas-Salas, A. Rajan, C. Chen, M. D. Perrin, J. Debes, D. Golimowski, D. C. Hines, M. N'Diaye, G. Schneider, D. Mawet, C. Marois, and R. Soummer, "Archival legacy investigations of circumstellar environments: overview and first results," Proc. SPIE **9143**, 914357 (2014).
4. J. B. Hagan, E. Choquet, R. Soummer, and A. Vigan, "ALICE Data Release: A Revaluation of HST-NICMOS Coronagraphic Images," Astrophys. J. **155**(4), 179 (2018).
5. J. R. Crepp, A. D. Van den Heuvel, and J. Ge, "Comparative Lyot coronagraphy with extreme adaptive optics systems," Astrophys. J. **661**(2), 1323–1331 (2007).
6. J. W. Goodman, *Introduction to Fourier Optics*, 2ed. (McGraw-Hill, 1996).
7. O. Guyon, E. A. Pluzhnik, M. J. Kuchner, B. Collins, and S. T. Ridgway, "Theoretical limits on extrasolar terrestrial planet detection with coronagraphs," Astrophys. J., Suppl. Ser. **167**(1), 81–99 (2006).
8. K. Iizuka, *Engineering Optics* (Springer, 1987).
9. D. Lafreniere, C. Marois, R. Doyon, D. Nadeau, and E. Artigau, "A new algorithm for point-spread function subtraction in high-contrast imaging: a demonstration with angular differential imaging," Astrophys. J. **660**(1), 770–780 (2007).
10. B. Lyot, "The Study of the Solar Corona and Prominences without Eclipses," Mon. Not. R. Astron. Soc. **99**(8), 580–594 (1939).
11. C. Marois, D. Lafrenière, R. Doyon, B. Macintosh, and D. Nadeau, "Angular differential imaging: a powerful high-contrast imaging technique," Astrophys. J. **641**(1), 556–564 (2006).
12. J. E. Oti, V. F. Canales, and M. P. Cagigal, "Pure amplitude masks for exoplanet detection with the optical differentiation coronagraph," Astrophys. J. **662**(1), 738–743 (2007).
13. N. Roddier, "Atmospheric wavefront simulation using Zernike polynomials," Opt. Eng. **29**(10), 1174–1180 (1990).
14. G. Schneider, in S. Arribas, A. Koekemoer, and B. Whitmore, eds., p. 249 (HST Calibration Workshop Space Telescope Science Institute, 2002).
15. G. Schneider, A.B. Schultz, S. Malhotra, and I. Dashevsky, in Instrument Science Report NICMOS 2005-001, Space telescope Institute, NASA (2005).
16. E. Serabyn, D. Mawet, and R. Burruss, "An image of an exoplanet separated by two diffraction beamwidths from a star," Nature **464**(7291), 1018–1020 (2010).
17. A. Sivaramakrishnan, C. D. Koresko, R. B. Makidon, T. Berkefeld, and M. J. Kuchner, "Ground-based coronagraphy with high-order adaptive optics," Astrophys. J. **552**(1), 397–408 (2001).
18. R. Soummer, A. Ferrari, C. Aime, and L. Jolissaint, "Speckle noise and dynamic range in coronagraphic images," Astrophys. J. **669**(1), 642–656 (2007).
19. R. Soummer, L. Pueyo, and J. Larkin, "Detection and characterization of exoplanets and disks using projections on Karhunen-Loève eigenimages," Astrophys. J. **755**(2), L28 (2012).
20. P. J. Valle, A. Fuentes A, V. F. Canales, M. A. Cagigas, I. Villo-Perez, and M. P. Cagigal, "Digital coronagraph algorithm," OSA Continuum **1**(2), 625–633 (2018).